

# Compton Imaging of MeV Gamma-Rays with the Liquid Xenon Gamma-Ray Imaging Telescope (LXeGRIT)

E. Aprile<sup>a</sup>, A. Curioni<sup>a, 1</sup>, K.L. Giboni<sup>a</sup>, M. Kobayashi<sup>a, 2</sup>,  
U.G. Oberlack<sup>b</sup>, S. Zhang<sup>a, 3</sup>

<sup>a</sup> *Columbia Astrophysics Laboratory and Physics Department, Columbia University, New York, NY, USA*

<sup>b</sup> *Dept. of Physics & Astronomy, Rice University, Houston, TX, USA*

---

## Abstract

The Liquid Xenon Gamma-Ray Imaging Telescope (LXeGRIT) is the first realization of a liquid xenon time projection chamber for Compton imaging of MeV  $\gamma$ -ray sources in astrophysics. By measuring the energy deposit and the three spatial coordinates of individual  $\gamma$ -ray scattering points, the location of the source in the sky is inferred with Compton kinematics reconstruction. The angular resolution is determined by the detector's energy and spatial resolutions, as well as by the separation in space between the first and second scattering. The imaging response of LXeGRIT was established with  $\gamma$ -rays from radioactive sources, during calibration and integration at the Columbia Astrophysics Laboratory, prior to the 2000 balloon flight mission. In this paper we describe in detail the various steps involved in imaging sources with LXeGRIT and present experimental results on angular resolution and other parameters which characterize its performance as a Compton telescope.

---

## Introduction

The Liquid Xenon Gamma Ray Imaging Telescope (LXeGRIT) is a prototype of Compton telescope (CT) based on a liquid xenon time projection chamber (LXeTPC), which combines good energy resolution with imaging of individual

---

<sup>1</sup> Present address: Yale University, Physics Dept., New Haven, CT, USA

<sup>2</sup> Present address: Waseda University, Tokyo, Japan

<sup>3</sup> Present address: High Energy Astrophysics Lab, Institute of High Energy Physics, Beijing, China

MeV  $\gamma$ -ray interactions with submillimeter position resolution (Sec. 1). A CT images  $\gamma$ -ray sources in the energy range from few 100 keV to more than 10 MeV, reconstructing the direction of individual  $\gamma$ -rays through Compton kinematics. The scatter angle on a free electron ( $\bar{\varphi}$ ) is given by the Compton formula

$$\cos \bar{\varphi} = 1 + \frac{1}{W_0} - \frac{1}{W_1}, \text{ with: } W_i = \frac{E_i}{m_e c^2} \quad (1)$$

where  $m_e c^2 = 0.511$  MeV,  $E_0$  is the initial energy and  $E_1$  is the energy of the scattered  $\gamma$ -ray. Fig. 1 helps illustrating the principle of Compton imaging. A

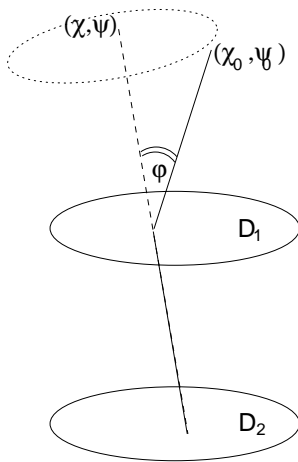


Fig. 1. Principle of a Compton telescope

$\gamma$ -ray from a source at position  $(\chi_0, \psi_0)$  Compton scatters in the plane  $D_1$  by the (true) angle  $\varphi$  and is stopped in the plane  $D_2$ ;  $\varphi$  is estimated from Eq. 1. The time sequence of the interactions needs also be known (Sec. 2). Interaction positions are measured in both planes and give the direction of the scattered photon  $(\chi, \psi)$ . The direction of an individual  $\gamma$ -ray is then determined to an *event circle* with radius  $\bar{\varphi}$  around the direction  $(\chi, \psi)$ . This ambiguity stems from the non-measurement of the direction of the scattered electron. After collection of many source events, intersection of all event circles defines the source position (Fig. 2). While back-projection of event circles on the sky is useful in visualizing the basic measurement principle, it is not the optimum method to perform Compton imaging. In fact, it doesn't include the probability distribution for scatter angles  $d\sigma/d\bar{\varphi}$  for photons from a source at given location and energy, i.e. the frequency of occurrence of event circles with a given opening angle. Fig. 2 illustrates how this additional information can be exploited in a 3D data space consisting of  $(\chi, \psi, \bar{\varphi})$ , where a point source defines a cone-like structure with half opening angle of  $45^\circ$  centered on the source position, with a density along the  $\bar{\varphi}$  dimension given by the Klein-Nishina cross section convolved with factors that result from the detector geometry and detector thresholds. Compton imaging of  $\gamma$ -sources is discussed in detail in Sec. 3 and

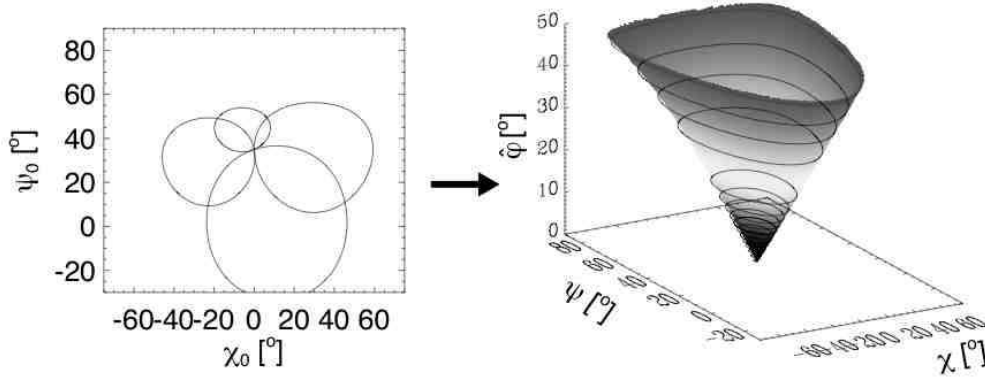


Fig. 2. Event circles for a point source (left) and the corresponding response function in the 3D imaging data space of an ideal classical Compton telescope (right). A point source describes a cone with half-opening angle of  $45^\circ$ . The density along the scatter angle dimension corresponds to the Klein-Nishina cross section and describes the density of circles of radius  $\phi$  in the event circle representation [1].

examples are given in Sec. 4.

## 1 The LXeGRIT Compton Telescope

For a detailed description of LXeGRIT and its performance as an imaging calorimeter, see [2,3,4]. In this section we summarize those aspects most relevant to Compton imaging.

The fiducial volume of the LXeTPC is a box with dimensions  $18.6 \times 18.6 \times 7 \text{ cm}^3$  (in the  $x$ ,  $y$ ,  $z$  coordinates respectively), filled with high purity LXe. At a temperature of  $T = -95^\circ \text{ C}$  the density of LXe is  $2.85 \text{ g cm}^{-3}$  [5] and the attenuation length for 1 MeV  $\gamma$ -rays in LXe is  $\sim 6.2 \text{ cm}$  [6]. When a  $\gamma$ -ray interacts in the fiducial volume, both scintillation light and ionization charge are produced efficiently, with  $W$ -values of  $W_{\text{ph}} = 24 \text{ eV}$  [7] and  $W_e = 15.6 \text{ eV}$  [8]. The VUV (178 nm) scintillation photons are detected by four photomultiplier tubes (PMTs), which provide the event trigger and the initial time,  $t_0$ . The PMTs<sup>4</sup> are coupled to the LXe volume via quartz windows. The ionization electrons drift under an applied electric field of  $1 \text{ kV/cm}$ , inducing a signal on two parallel wire planes, after passing a Frisch grid. There are 62 wires in each plane and the pitch of the wires is 3 mm. The location of the hit wire(s) in the two wire planes provide the  $x$  and  $y$  coordinates in the TPC reference frame, while the time, measured starting from  $t_0$ , gives the interaction depth ( $z$  coordinate). The wires are transparent to the drifting charge, which is finally collected by one of four independent anodes, and the amplitude measures the

<sup>4</sup> 2" Electron Tubes 9813QA.

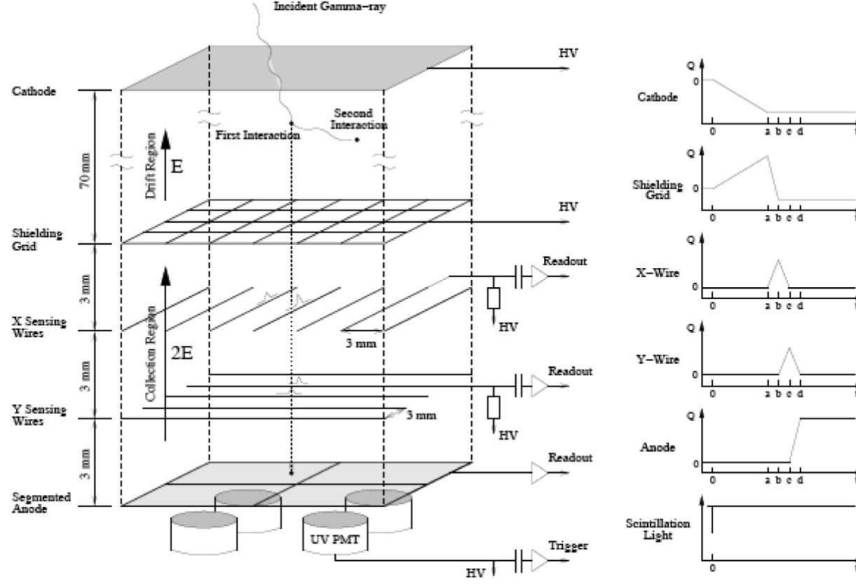


Fig. 3. Schematic of the LXeTPC readout structure (not to scale) with corresponding light trigger and charge pulse shapes. From [3].

energy deposited in the interaction. A schematic of the readout structure and light trigger of LXeGRIT is shown in Fig. 3.

A reliable Monte Carlo (MC) simulation of the detector has been developed and tested to produce accurate results up to several MeV[3]. For a generic  $\gamma$ -ray event, the LXeGRIT output is  $(E_1, x_1, y_1, z_1); \dots; (E_n, x_n, y_n, z_n)$  where  $n$  is the event multiplicity, i.e. the number of detected interactions once the finite spatial resolution and energy threshold ( $\sim 150$  keV for a single interaction) are accounted for.

### 1.1 Position resolution

The interaction location in the LXeTPC is obtained from the wire signature. With a wire pitch of 3 mm, the spatial resolution is  $0.87$  mm ( $\text{rms} = 3 \text{ mm}/\sqrt{12}$ ) in  $x - y$ , if only a single wire signal is detected for each coordinate. For LXeGRIT this is the typical case for energy deposits  $< 0.3$  MeV [9]. The reconstructed image of a collimated beam of  $\gamma$ -rays ( $0.662$  MeV) photoabsorbed in the sensitive volume is shown in Fig. 4, both in the  $x - y$  and in the  $x - z$  views. The  $^{137}\text{Cs}$  source was located above the TPC, collimated to a beam with 3 mm diameter in the  $x - y$  plane by a lead collimator 15 cm thick. The position resolution in the  $z$ -coordinate is estimated to be about  $0.25$  mm (1 sigma). It is derived as the difference in drift times measured independently on the  $x$  and  $y$  wires for the same interaction, as shown in Fig. 5-left. Assuming two independent measurement with Gaussian errors (neglecting the

uncertainty in the common trigger),  $\sigma = 0.35\text{mm}/\sqrt{2} \approx 0.25$  mm. The  $z$ -distribution of photoabsorbed events from the same collimated  $^{137}\text{Cs}$  source is shown in Fig. 5-*right*, well reproducing the expected exponential attenuation. This spatial resolution fulfills the requirement of a fine grained CT, where a typical separation between interactions is in the few cm range and the linear extension of the charge cloud due to MeV energy deposits is typically less than 1 mm.

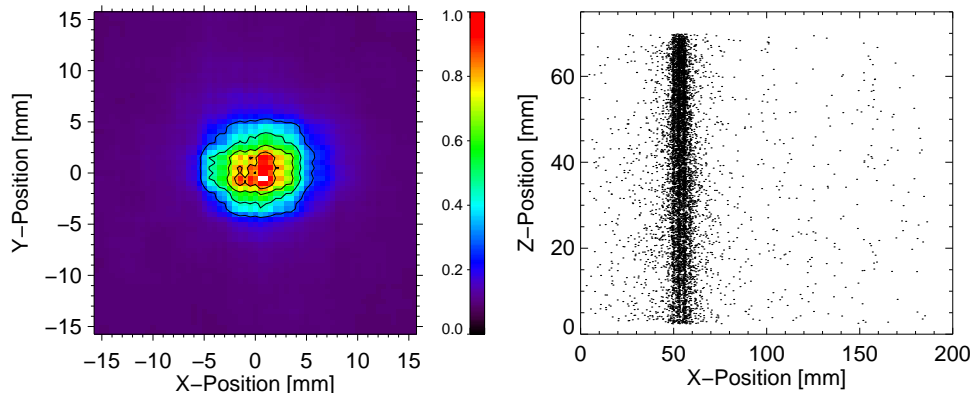


Fig. 4. Image of the  $\gamma$ -beam from a collimated  $^{137}\text{Cs}$  source on top of the TPC. *Left*: projection in the  $x - y$  plane. The coordinates have been re-defined in order to have the source image centered at  $x = 0$ ,  $y = 0$ . *Right*: side view ( $x - z$  plane) of the same  $\gamma$ -beam.

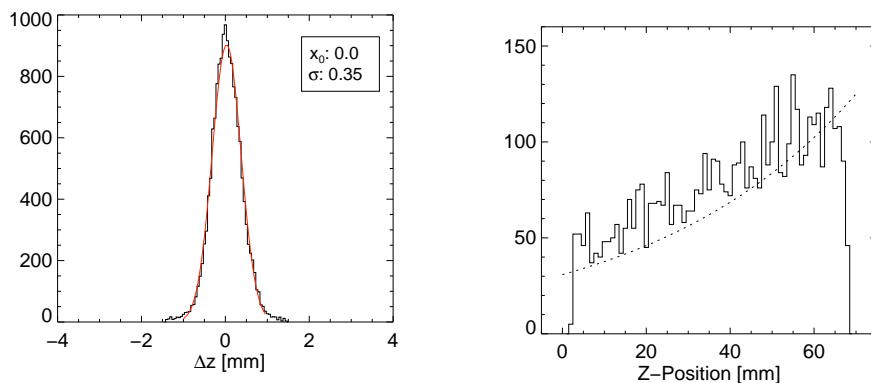


Fig. 5. *Left*: difference between the  $z$ -position as determined from the  $x$  and  $y$  wires. *Right*:  $z$ -distribution for a collimated  $^{137}\text{Cs}$  source sitting on top of the LXeTPC. Events in the full energy peak have been selected; superimposed (*dashed line*) the exponential attenuation for 0.662 MeV photons. The slight discrepancy at  $z \sim 60$  mm is mainly due to the  $z$  dependent light trigger efficiency, which is not corrected for.

## 1.2 Energy resolution

The energy response is determined to be linear over the energy range from 0.5 to 4.4 MeV, covered by the available calibration sources <sup>5</sup>, and is shown in Fig. 6-*left*. The energy dependence of the energy resolution is shown in Fig. 6-*right* and is described as

$$\Delta E/E(FWHM) = \sqrt{\frac{P_1^2}{E} + \frac{P_2}{E^2}}$$

where  $P_1$  accounts for the intrinsic energy resolution from the statistics of charge carriers in LXe;  $1/\sqrt{E}$  reproduces the energy dependence expected from Poisson statistic;  $P_2$  accounts for contributions which are independent of energy (*noise term*). The noise term parameterizes electronic noise, errors in fitting the anode wave function, shielding inefficiencies of the wires structure etc. In practice it is well described considering the electronic noise only (63 keV FWHM, which corresponds to about 1000 equivalent noise charge, as in [4]). The intrinsic energy resolution is 8.3% at 1 MeV, in good agreement with previous measurements in LXe at the same drift field (1 kV/cm), from gridded ionization chambers of much smaller fiducial volume [10].

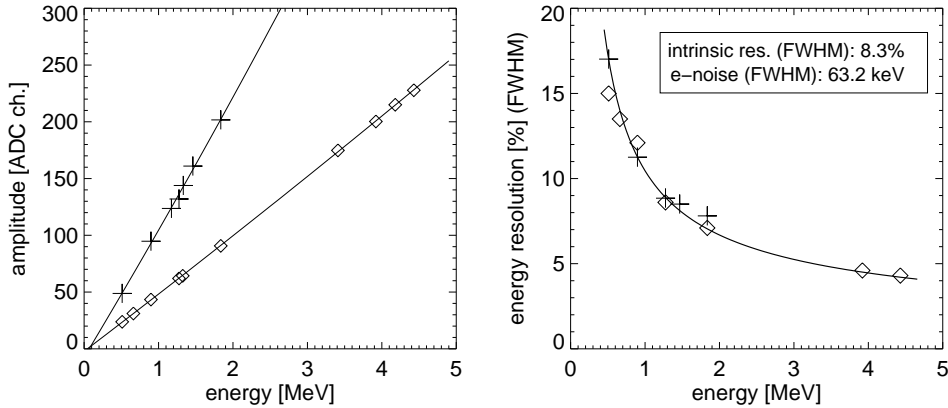


Fig. 6. *Left*: linearity plot for ADC channel vs. energy in MeV for both the 1999 (*open diamonds*) and the 2000 (*crosses*) LXeGRIT electronics configuration. The gain in 2000 was about twice the gain in 1999. *Right*: energy resolution versus energy, showing the  $1/\sqrt{E}$  dependence expected from Poisson statistic corrected by a constant term.

<sup>5</sup> <sup>22</sup>Na(0.511 and 1.275 MeV), <sup>137</sup>Cs(0.662 MeV), <sup>88</sup>Y(0.898 and 1.836 MeV), <sup>60</sup>Co(1.173 and 1.332 MeV), <sup>40</sup>K(1.465 MeV), Am-Be (4.43 MeV).

## 2 Gamma ray tracking

The most general interaction sequence useful for Compton imaging is a first Compton scatter followed by full absorption of the scattered  $\gamma$ -ray in one or more interactions <sup>6</sup>. In LXeGRIT, a large fraction of multi-site events has only two interactions (Compton scatter followed by photoabsorption). The fraction of events with more than 3 interactions is at most 5% of the fully contained events for energies below 5 MeV and is not considered in the following. The two cases for 2- or 3- interactions are treated separately in Sec. 2.1 and Sec. 2.2.

Events with interactions other than Compton scattering and photoabsorption are not considered here for Compton imaging. The relative fraction of these events increases with energy and becomes dominant above  $\sim 5$  MeV. The cross section for pair production turns on at 1.022 MeV and, in LXe, equals the Compton cross section at  $\sim 6$  MeV. Relativistic electrons lose energy both by ionization and by radiation of secondary photons (Bremsstrahlung), which, if of sufficiently high energy, may be detected at a separate location. For electrons the radiative energy loss overcomes the one due to ionization above the *critical energy*  $E_c = 610 \text{ MeV} / (Z + 1.24)$  for liquids and solids [15]. For Xe,  $Z = 54$  and  $E_c = 11 \text{ MeV}$ . Experimentally, we observe considerable modifications to the energy spectrum for the 4.4 MeV Am-Be calibration source.

### 2.1 2-site events

In the case of 2-site events, assuming no prior knowledge the right sequence can be guessed with a 50% success rate. This improves using the *energy sharing* between the two interactions that is, in many cases, highly asymmetric. For LXeGRIT, the argument goes like this: for energies larger than  $\sim 2$  MeV a  $\gamma$ -ray is more likely to be stopped in the fiducial volume with only two interactions if it does lose a large fraction of the initial energy in the *first* interaction. If the energy lost in the first interaction is small, the scattered photon will most likely interact more than once before being absorbed, i.e. would be classified as a 3(+)-site event. Fig. 7 shows the  $E_1$  and  $E_2$  energy spectra for 0.662 MeV ( $^{137}\text{Cs}$ ), 0.898 and 1.836 MeV ( $^{88}\text{Y}$ ) photons. The  $^{137}\text{Cs}$  source was collimated to a beam with a lateral spread of  $\sim 3$  mm, which allows us to tag the first interaction as the one within the collimator aperture. The  $^{88}\text{Y}$  source was at a distance of 2 m above the detector, without any collimation. Since the source position is known, it is possible to use Compton imaging (Sec. 3) and track each  $\gamma$ -ray assuming the two possible sequences. The sequence which gives the correct source position is then chosen as the true

---

<sup>6</sup> For additional reading on  $\gamma$ -ray tracking, see e.g. [11,12,13,14]

one. For 1.836 MeV the  $E_1$  and  $E_2$  spectra almost mirror each other (Fig. 7-*right*), and the situation  $E_1 > E_2$  is clearly the most likely. At lower energies (0.662 and 0.898 MeV) the two spectra are much more similar and the  $E_1/E_2$  asymmetry is no more a good argument. The minimum in the  $E_1$  spectrum, clearly visible for all the three energies, corresponds to  $90^\circ$  scatter angle (the corresponding  $E_1 = E_{tot}^2/(m_e c^2 + E_{tot})$  is marked with a vertical dashed line). It is a geometrical artifact, due to the direction of the incident  $\gamma$ -rays along the detector  $z$  axis, such that for a  $\gamma$ -ray scattered at  $90^\circ$   $z_1 \simeq z_2$ , while a minimum separation of about 3 mm along the  $z$ -axis is required to ensure a good energy determination [2]. In Fig. 8-*left* the ratio  $\langle E_1 \rangle / E_\gamma$  is plotted vs.  $E_\gamma$  for MC data, where  $\langle E_1 \rangle$  is the mean of the first energy deposition and  $E_\gamma$  is the nominal energy of the  $\gamma$ -ray. The trend is quite clear:  $\langle E_1 \rangle / E_\gamma$  increases with  $E_\gamma$  and  $\langle E_1 \rangle / E_\gamma \geq 75\%$  for  $E_\gamma \geq 2$  MeV. Fig. 8-*left* is

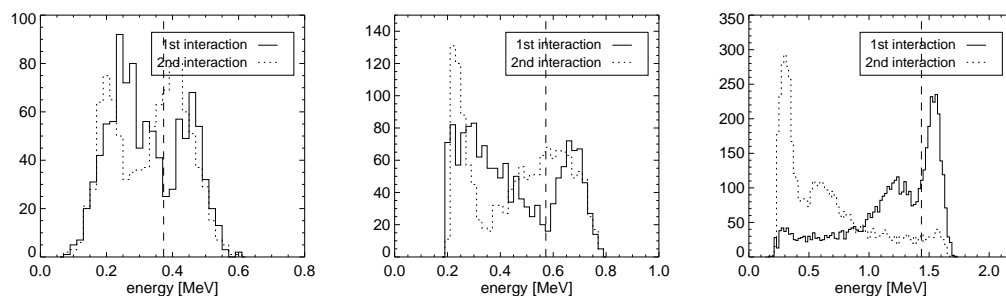


Fig. 7.  $E_1$ ,  $E_2$  distribution for fully contained 2-site events. From left to right: 0.662 MeV ( $^{137}\text{Cs}$ ), 0.898 and 1.836 MeV ( $^{88}\text{Y}$ ).

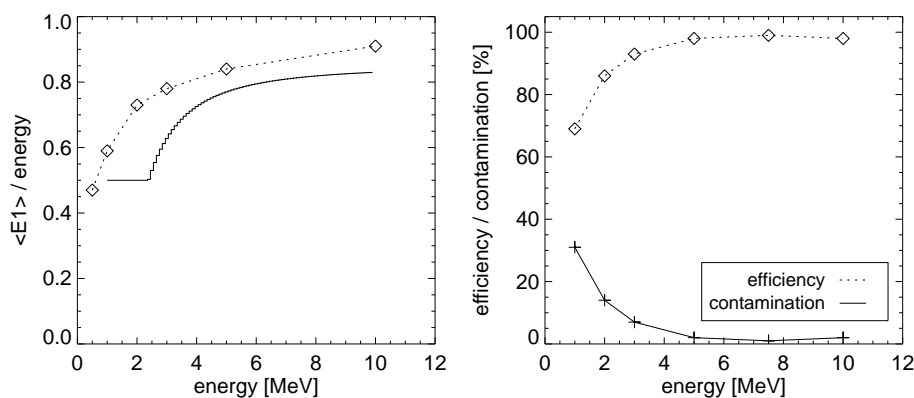


Fig. 8. *Left*:  $\langle E_1 \rangle / E_\gamma$  vs.  $E_\gamma$ , from MC data. Superimposed  $f(E_\gamma)$  as defined in Eqs. 2-3 *Right*: Efficiency and contamination in sequencing 2-site events according to the procedure described in Sec. 2.1.

suggestive of an optimized selection on the energy sharing, requiring the ratio

$E_1/E_{tot}$  to be larger than some value  $f(E_{tot})$

$$f(E_{tot}) = 0.85 \left( 1 - \frac{2}{E_{tot}^2} \right) \quad ; \quad E_{tot} > 2.4 \text{ MeV} \quad (2)$$

$$f(E_{tot}) = 0.5 \quad ; \quad 1 \text{ MeV} \leq E_{tot} \leq 2.4 \text{ MeV} \quad (3)$$

shown in Fig. 8-*left* with  $E_{tot} = E_\gamma$ . Fig. 8-*right* gives efficiency and contamination for this sequencing procedure in the energy range 1-10 MeV. The efficiency is as high as 86% at 2 MeV and saturates ( $\geq 98\%$ ) at 5 MeV. Below 1 MeV no optimum criterion for sequencing 2-site events has been found.

## 2.2 Multi-site events

When more than two interactions are available, the time sequence is, in principle, univocally determined by Compton kinematics. In the general case of a  $\gamma$ -ray which undergoes  $N - 1$  Compton scatters and is photoabsorbed in the  $N^{th}$  interaction energy and momentum conservation is written as

$$E_{i-1}^\gamma = E_i^\gamma + E_i^e \quad ; \quad \vec{p}_{i-1}^\gamma = \vec{p}_i^\gamma + \vec{p}_i^e \quad (4)$$

with  $E_i^\gamma$  ( $i = 0, \dots, N - 1$ ) and  $E_i^e$  ( $i = 1, \dots, N$ ) the energy of the  $\gamma$ -ray and the scattered electron after interaction  $i$ ;  $E_0^\gamma$  is the energy of the incoming photon and  $\vec{p}_i$  are the corresponding momenta. The electron scatter angle is not measured and is ignored in the following. For the photon scatter angle  $\varphi$

$$\cos \varphi_i = 1 + \frac{1}{W_i} - \frac{1}{W_{i+1}}, \text{ with: } W_i = \frac{E_i^\gamma}{m_0 c^2} \quad (5)$$

For a given interaction sequence, the interaction locations determine geometrically  $N - 2$  photon scatter angles  $\varphi_{\text{geo } i}$  ( $i = 2, \dots, N - 1$ ):

$$\cos \varphi_{\text{geo } i} = \frac{\vec{u}_i \cdot \vec{u}_{i+1}}{|\vec{u}_i| |\vec{u}_{i+1}|} \quad (6)$$

where  $\vec{u}_i = (x_i - x_{i-1}, y_i - y_{i-1}, z_i - z_{i-1})$ .

$N - 1$  Compton scatter angles  $\bar{\varphi}_i$  are measured by the energy deposits according to equation 5, noting that  $E_i^\gamma = \sum_{j=i+1}^N E_j$  ( $i = 0, \dots, N - 1$ ). This redundant information allows testing of the sequence of the interaction points based solely on kinematics. A straightforward test statistic consists in summing the

differences of the scatter angles quadratically, weighting the summands with the measurement errors:

$$T_\varphi = \frac{1}{N-2} \sum_{i=2}^{N-1} \frac{(\cos \bar{\varphi}_i - \cos \varphi_{\text{geo } i})^2}{\sigma_i^2} \quad (7)$$

$$\text{with: } \sigma_i^2 = \sigma_{\cos \bar{\varphi}, i}^2 + \sigma_{\cos \varphi_{\text{geo}, i}}^2$$

Ideally, the test statistic would be zero for the correct sequence if the photon is fully contained. With measurement errors,  $T'_\varphi$  is always greater than zero, but the correct interaction sequence is still most likely to produce the minimum value of the test statistic. A straightforward interpretation as a reduced  $\chi^2$  distribution is not possible due to the non-Gaussian shape of the probability distribution in  $\bar{\varphi}$ . For each triplet of interactions  $\sigma_{\cos \bar{\varphi}}$  and  $\sigma_{\cos \varphi_{\text{geo}}}$  then are computed

$$\sigma_{\cos \varphi_{\text{geo}, i}}^2 = \sum_{k=1}^3 \left\{ \left( \frac{u_{i+1, k}}{|\vec{u}_i| \cdot |\vec{u}_{i+1}|} - \frac{u_{i, k} \cos \varphi_{\text{geo}}}{|\vec{u}_i|^2} \right)^2 + \left( \frac{u_{i, k}}{|\vec{u}_i| \cdot |\vec{u}_{i+1}|} - \frac{u_{i+1, k} \cos \varphi_{\text{geo}}}{|\vec{u}_{i+1}|^2} \right)^2 \right\} \cdot \sigma_k^2 \quad (8)$$

with:  $k$  spatial coordinate index and

$\sigma_k$  position uncertainty on each coordinate

$$\sigma_{\cos \bar{\varphi}, i}^2 = \frac{1}{W_i^4} \cdot \sigma(W_i - W_{i+1})^2 + \left( \frac{1}{W_i^2} - \frac{1}{W_{i+1}^2} \right)^2 \cdot \sigma(W_{i+1})^2 \quad (9)$$

We consider here only the case of 3 interactions, by far the most likely. There are six (3!) possible sequences to start with, i.e. assuming no additional knowledge the right sequence is chosen 17% of the times. The efficiency of this procedure is shown in Fig. 9-*left*, using MC data. It is  $\sim 55\%$  at 2 MeV and exceeds 60% above 5 MeV. In LXeGRIT the energy resolution is the limiting factor. The fraction of wrongly sequenced events (*contamination*) is also shown in Fig. 9-*left*. In this case, since no event is rejected, it is just the complement to 1 of the efficiency. It is worthwhile to note that the most frequent confusion of the interaction sequence involves the swap of second and third interaction, while the first interaction is properly found. Such events, counted here under “confusion”, remain usable for imaging if the separation between second and third interaction is considerably shorter than the separation of first and second interaction. In this case, the wrong sequence leads to tails in angular resolution but not to a “conversion” of source photons into background photons. Assuming the efficiency shown in Fig. 9-*left* as an upper limit, the algorithm performance can be improved applying further selections *a posteriori*, with the goal of keeping the efficiency as close as possible to the one in Fig. 9-*left* while reducing the contamination.

The most powerful variable is  $E_1/E_{tot}$ , where  $E_1$  is the energy deposited in the *first* interaction <sup>7</sup>. Fig. 10 shows  $E_1/E_{tot}$  for the 0.898 and 1.836 MeV  $^{88}\text{Y}$  line (experimental data), when all the events are considered and selecting only events with the time sequence correctly identified, i.e. events for which the source is correctly imaged. At 0.898 MeV there is no clear correlation between  $E_1/E_{tot}$  and finding the right sequence, but at 1.836 MeV a large fraction of wrongly reconstructed events shows up at  $E_1/E_{tot} < 0.3$ . The impact of selecting  $E_1/E_{tot} > 0.3$  has been studied over the energy range 0.5-10 MeV using MC data. The efficiency of the  $\gamma$ -tracking procedure combined with this *a posteriori* selection is shown in Fig. 9-*right* together with the contamination, here defined as the fraction of events (in the full energy peak) which are wrongly sequenced and have  $E_1/E_{tot} > 0.3$ . This technique works well above 2 MeV, while at lower energies the reduction in efficiency combined with poor rejection power makes it counterproductive, as also seen in Fig. 10-*left*.

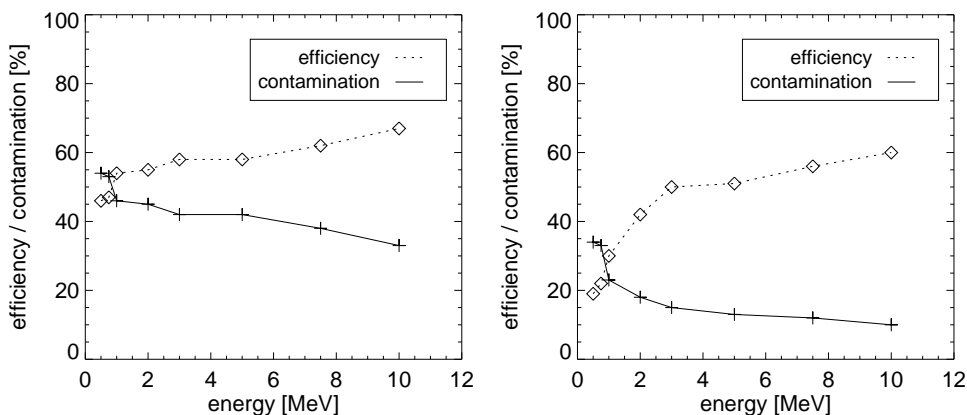


Fig. 9. Efficiency and contamination in the reconstruction of the correct time sequence for 3-site event, as calculated using MC data and the actual algorithm used for experimental data. *Left*: without applying any further selection. In this case events can only be *correctly* or *wrongly* sequenced, since no event is rejected. *Right*: selecting  $E_1/E_{tot} > 0.3$  *a posteriori*. The contamination fraction is here defined as the fraction of events wrongly sequenced which have  $E_1/E_{tot} > 0.3$ .

### 3 Compton imaging

#### 3.1 Angular resolution

If the source position is known, two independent measurements of the first Compton scatter angle ( $\bar{\varphi}$  and  $\varphi_{\text{geo}}$ ) are given. The difference between the two

<sup>7</sup> *First* according to the  $\gamma$ -tracking algorithm

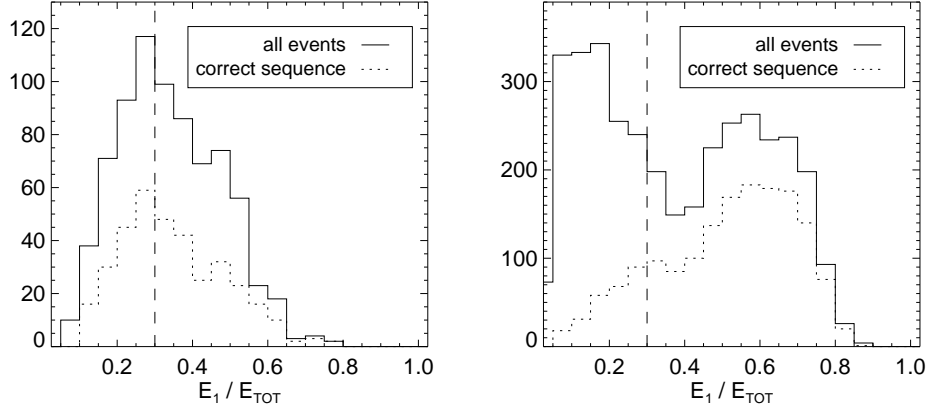


Fig. 10.  $E_1/E_{tot}$  for 0.898 (*left*) and 1.836 (*right*) MeV  $\gamma$ -rays. From experimental data, imposing full energy containment.

gives the measure of the angular resolution (ARM). In this section ARM and  $1\text{-}\sigma$  angular resolution are interchangeable. Three sources of error limit the angular resolution: *energy resolution*, which limits the precision in measuring  $\bar{\varphi}$ ; *position resolution*, which limits the precision in measuring  $\varphi_{\text{geo}}$ ; and *Doppler broadening*.

The uncertainty on the scatter angle due to the energy resolution is:

$$\Delta\bar{\varphi} = \frac{m_e c^2}{\sin \bar{\varphi}} \sqrt{\left(\frac{\Delta E_1}{E_{tot}^2}\right)^2 + \left(\frac{E_1(E_1 + 2E_2)\Delta E_2}{E_{tot}^2 E_2^2}\right)^2} \quad (10)$$

where  $E_{tot}$  is the initial energy of the  $\gamma$ -ray,  $E_1$  the energy deposited in the first interaction,  $E_2 = E_{tot} - E_1$ ; in Eq. 10 there are only two free parameters, e.g.  $\bar{\varphi}$  and  $E_{tot}$ . Its behavior as a function of  $\bar{\varphi}$  and of  $E_{tot}$  is shown in Fig. 11. The curve for the  $\bar{\varphi}$  dependence is obtained for  $E_{tot}=1.836$  MeV, the one for the  $E_{tot}$  dependence is obtained integrating over  $\bar{\varphi} < 60^\circ$  according to the Klein-Nishina cross section. An energy threshold of 150 keV and an energy resolution of 10% /  $\sqrt{E}$  [MeV] (FWHM) have been assumed.

The uncertainty on the direction of the scattered  $\gamma$ -ray,  $\Delta\varphi_{\text{geo}}$ , assuming a separation between the first two interaction locations  $|\vec{u}|$  large compared to  $\sigma_x$ ,  $\sigma_y$  and  $\sigma_z$ , is given by

$$\Delta\varphi_{\text{geo}} = \frac{\sqrt{2}}{|\vec{u}|} \sqrt{(\Delta\varphi_{\text{geo}})_x^2 + (\Delta\varphi_{\text{geo}})_y^2 + (\Delta\varphi_{\text{geo}})_z^2} \quad (11)$$

with  $(\Delta\varphi_{\text{geo}})_a = \frac{\sqrt{2}}{|\vec{u}|} \sigma_a \sqrt{1 - \left(\frac{\vec{u} \cdot \hat{a}}{|\vec{u}|}\right)^2}$ ,  $a = x, y, z$ . In Fig. 11  $\Delta\varphi_{\text{geo}}$  is shown for  $|\vec{u}| = 30$  mm.

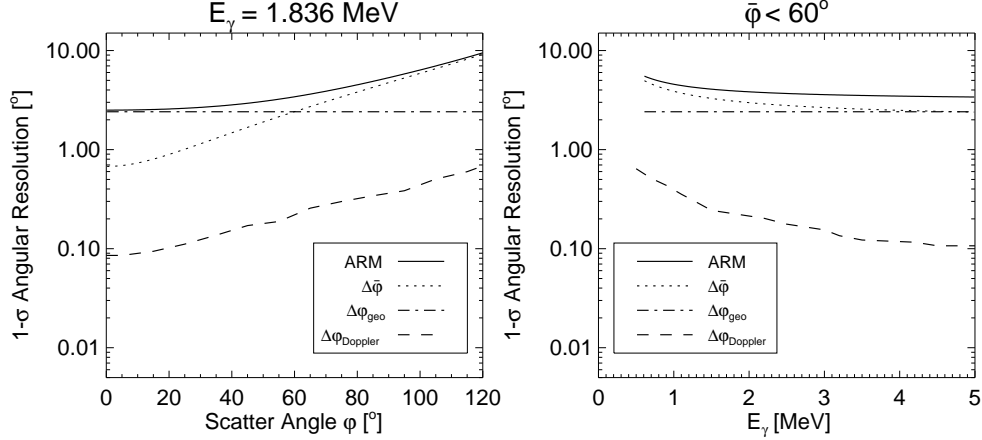


Fig. 11. Expected angular resolution for LXeGRIT;  $\Delta\bar{\varphi}$  and  $\Delta\varphi_{\text{geo}}$  have been obtained using Eqs. 10, 11 and combined to give the final ARM according to Eq. 12. *Left*: expected angular resolution vs. scatter angle  $\varphi$  for a fixed energy (1.836 MeV). *Right*: expected angular resolution for LXeGRIT vs. energy, selecting  $\bar{\varphi} < 60^\circ$ , i.e. forward scattering.

The Compton formula in Eq. 1 gives the scattering angle *if* the incident photons were to interact with stationary free electrons. Doppler broadening constitutes an irreducible limitation to angular resolution for a CT and its effect is larger for target materials of larger atomic number, such as Ge or Xe, compared to Si or liquid scintillators [16]. For low energy (few 100 keV)  $\gamma$ -rays, the uncertainty in the scatter angle due to Doppler broadening contributes significantly to the overall ARM. Once energy resolution and position resolution are taken into account, Doppler broadening plays a rather negligible role for LXeGRIT (Fig. 11), which is designed to image  $\gamma$ -rays of energy 0.5 MeV or higher.

Neglecting Doppler broadening, the overall angular resolution  $\Delta\varphi$  is defined as

$$\Delta\varphi = \sqrt{\Delta\varphi_{\text{geo}}^2 + \Delta\bar{\varphi}^2} \quad (12)$$

At 1.836 MeV the  $1\sigma$  angular resolution is about  $3^\circ$  for scatter angles up to  $60^\circ$ , improving for more forward scattering. The dependence of  $\Delta\varphi$  on the interaction separation is shown in Fig. 12-*right*, for different position resolution. Given the typical separation of the order of few cm shown in Fig. 12-*left*, a mm position resolution is required for a good imaging performance.

The ARM spectra for real data, 1.836 MeV  $\gamma$ -rays, is shown in Fig. 13. For a realistic comparison with expectation, the analysis is based on MC data. In this way it is also possible to separate the response for 2- and 3-site events. The result for the energy band 0.5-10 MeV is shown in Fig. 14-*left*. In Fig. 14-*right* MC data and experimental data are compared for the lines: 0.662 ( $^{137}\text{Cs}$ ),

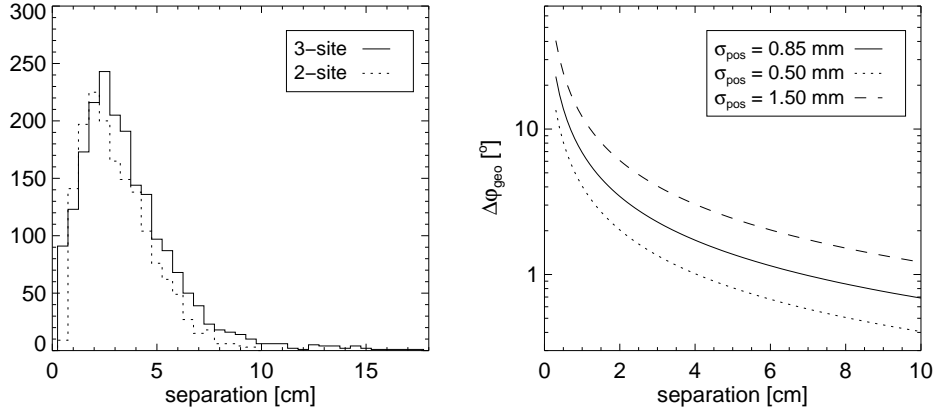


Fig. 12. *Left*: 3D separation between the first and the second interaction for 1.836 MeV fully contained  $\gamma$ -rays. *Right*: Angular spread  $\Delta\varphi_{\text{geo}}$  vs. 3D separation for different values of the position resolution. LXeGRIT achieves a position resolution of 0.85 mm.

0.898 ( $^{88}\text{Y}$ ), 1.275 ( $^{22}\text{Na}$ ) and 1.836 ( $^{88}\text{Y}$ ) MeV (2-site events), and 0.898, 1.275 and 1.836 MeV (3-site events).

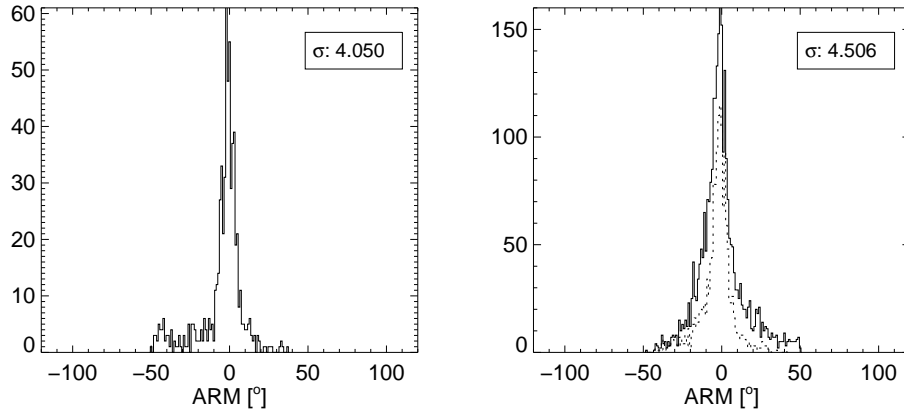


Fig. 13. ARM spectra for 1.836 MeV  $\gamma$ -rays ( $^{88}\text{Y}$  source). The standard deviation has been obtained fitting the ARM spectra with a Gaussian function. *Left*: 3-site events. *Right*: 2-site events. The dashed line indicates events with  $\bar{\varphi}$  restricted to less than  $70^\circ$ . This selection makes the ARM distribution sensibly narrower, getting rid of the extended tails due to large scatter angles. The standard deviation has been derived from this selected sample.

The angular resolution vs.  $\bar{\varphi}$  is shown in Fig. 15, from the same data (2- and 3-site events combined); the experimental points are compared to the expected angular resolution (as shown in Fig. 11-*left*), showing a good agreement. The expectation for a position resolution degraded to 2 mm is also shown; for small  $\bar{\varphi}$  the overall performance is compromised.

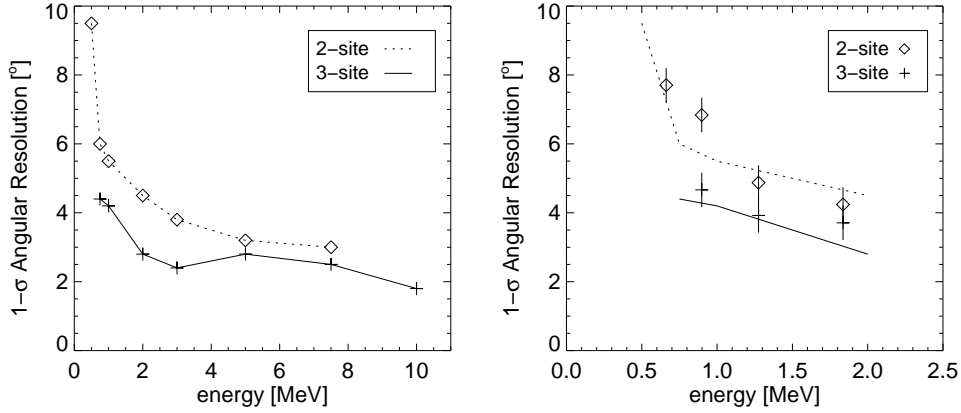


Fig. 14. ARM spread vs. energy obtained using accurate MC data and experimental data. The 2- and 3-site samples are shown separately. *Left*: MC data; the point at 0.5 MeV in the 3-site data and the one at 10 MeV in the 2-site data have been omitted because of very little statistical significance. Full energy containment has been imposed. *Right*: Experimental data: 0.662 ( $^{137}\text{Cs}$ ), 0.898 ( $^{88}\text{Y}$ ), 1.275 ( $^{22}\text{Na}$ ) and 1.836 ( $^{88}\text{Y}$ ) MeV for 2-site events, 0.898, 1.275 and 1.836 MeV for 3-site events. The corresponding MC curves have been superimposed.

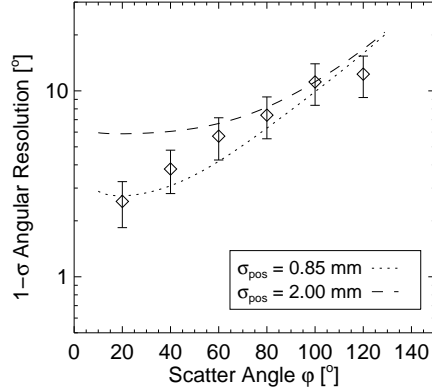


Fig. 15. Angular resolution vs. scatter angle for a sample of 1.836 MeV  $\gamma$ -rays, in  $\bar{\varphi}$  bins of  $20^\circ$ . Superimposed, the expected angular resolution assuming two different values for the position resolution. The expected LXeGRIT position resolution of about 0.85 mm agrees well with the data. A 2 mm position resolution, while still in good agreement with the data for scatter angles larger than  $60^\circ$ , is clearly ruled out by the two points at  $20^\circ$  and  $40^\circ$ , the only ones actually sensitive to  $\Delta\varphi_{\text{geo}}$ .

### 3.2 Maximum Likelihood Image Reconstruction

The imaging problem deals with the derivation of the intensity distribution of the *object region* from the observational data, which, for a Compton telescope, can be represented in a 3D binned data space consisting of the scatter direction

$(\chi, \psi)$  and the scatter angle  $\bar{\varphi}$ :

$$D_i = \sum_j R_{ij} f_j + b_i + N_i \quad (13)$$

where  $D_i$  is the observed number of counts,  $b_i$  the expected background, and  $N_i$  the statistical noise in the  $i^{th}$  bin in data space,  $R_{ij}$  is the instrumental response, i.e. the probability to detect a photon from the  $j^{th}$  pixel in the object region in the  $i^{th}$  bin in the data space, and  $f_j$  is the flux in the  $j^{th}$  pixel in the object region. We restrict ourselves in the following to maximum likelihood fitting of single or few point sources (plus background), scanning and testing a grid of image pixels for one source at a time. The probability of the observed data under a specific model  $\{f_j, b_i\}$  is given by the likelihood function  $L$ , defined by multiplying the probability of each bin

$$L = \prod_i P_i = \prod_i P(D_i | f_j, b_i) \quad (14)$$

As a counting experiment with fixed observing time the statistics in each bin is given by the Poisson distribution

$$\begin{aligned} P_i &= \frac{\omega_i^{D_i}}{D_i!} e^{-\omega_i} & \text{for } \omega_i > 0 \\ P_i &= 1 & \text{for } \omega_i = 0, D_i = 0 \\ P_i &= 0 & \text{for } \omega_i = 0, D_i > 0 \end{aligned} \quad (15)$$

where  $\omega_i = \sum_j R_{ij} f_j + b_i$  is the expected number of counts in the  $i^{th}$  bin and  $P_i$  the probability of having  $D_i$  counts in the  $i^{th}$  bin, given  $\omega_i$ .

Taking the logarithm of the likelihood function, one obtains

$$\log L = \sum_i D_i \log \omega_i - \sum_i \omega_i + C \quad (16)$$

where  $C = -\sum_i \log(D_i!)$  is a constant with respect to the parameters  $f_j$  and is therefore model independent and can be neglected. Maximizing  $L$  with respect to the flux distribution  $\{f_j\}$  for the intensity  $f_j$  results in the following set of equations:

$$\sum_i D_i \frac{\partial \omega_i}{\partial f_j} / \omega_i - \sum_i \frac{\partial \omega_i}{\partial f_j} = 0 \quad (17)$$

This is the general expression for maximum likelihood in binned mode. A possible choice to solve the system in Eq. 17 is the Newton-Raphson algorithm

[17], which separately estimates each pixel on the source parameters. The statistical significance is then obtained from  $-2 \log \lambda$ , where  $\lambda$  is the likelihood ratio of the two hypotheses background only and background plus source [18].  $-2 \log \lambda$  follows a  $\chi^2_3$  distribution for an unknown point source and a  $\chi^2_1$  distribution for a known source.

A different approach, known as *list mode* likelihood method, aims at reconstructing an image on an event-by-event basis. This method may be derived from the binned likelihood method by increasing the number of bins in the data space until each bin contains either 0 or 1 event. If only bins that contain an event are considered, Eq. 17 deals with events rather than bins. The probability to detect a photon from the  $j^{th}$  pixel of the object region in the  $i^{th}$  bin turns into the probability density for the  $i^{th}$  photon in the data space. The list mode maximum likelihood method is very useful in overcoming problems of storage in computer memory and in reducing the CPU time needed for the calculation for cases of sparsely populated dataspace, e.g., when each event contains multiple parameters relevant to the imaging problem. A detailed description of this technique is given in [19].

In the case of a CT, the equation in list mode can be derived directly from the one in binned mode. One defines the source position  $(\chi_0, \psi_0)$  in a 3D data space  $(\bar{\varphi}, \chi, \psi)$ , where  $\chi, \psi$  is some reference frame, e.g. longitude and latitude or right ascension and declination (Ra, Dec). The instrument response is equivalently given in a 3D data space as  $R^{(3)}(\chi, \psi, \bar{\varphi})$  or in a 2D data space as  $R^{(2)}(\bar{\varphi}, \varphi_{\text{geo}})$ . In the 3D data space  $R^{(3)}(\chi, \psi, \bar{\varphi}|\chi_0, \psi_0)$  has a conical shape with a half-opening angle of  $45^\circ$  and the vertex at the source location  $(\chi_0, \psi_0)$  (Fig. 2).  $R^{(2)}(\bar{\varphi}|\varphi_{\text{geo}})$  is given by the probability of measuring  $\bar{\varphi}$  for a given scatter angle  $\varphi_{\text{geo}}$ ; an example for LXeGRIT is shown in Fig. 16. The probability distribution is enhanced along the diagonal, i.e. for  $\bar{\varphi} = \varphi_{\text{geo}}$ , which is equivalent to having the ARM peak at  $0^\circ$ .  $R^{(3)}$  and  $R^{(2)}$  are connected through the relation

$$R^{(3)}(\chi, \psi, \bar{\varphi}|\chi_0, \psi_0) 2\pi \sin \varphi_{\text{geo}} d\varphi_{\text{geo}} = R^{(2)}(\bar{\varphi}|\varphi_{\text{geo}}) \cos \psi d\chi d\psi \quad (18)$$

We have presently implemented the list-mode likelihood method only without the background term, i.e. the expected number of counts in the  $i^{th}$  bin is now

$$\omega_i = \sum_j R_{ij}^{(3)} f_j \quad (19)$$

The logarithm of the likelihood function is written as

$$\log L = \sum_i D_i \log \left( \sum_j R_{ij}^{(3)} f_j \right) - \sum_{i,j} R_{ij}^{(3)} f_j + C \quad (20)$$

If the bin size is reduced until each bin has at most one count,  $D_i$  can only be 0 or 1. The first term in Eq. 20 is now the sum over events rather than bins. Introducing an index  $ie$  to indicate events and  $id$  to indicate bins, Eq. 20 can be rewritten as

$$\log L = \sum_{ie} \log \left( \sum_j R_{ie,j}^{(3)} f_j \right) - \sum_{id,j} R_{id,j}^{(3)} f_j + C \quad (21)$$

Approximating  $R^{(2)}(\bar{\varphi}, \varphi_{\text{geo}})$  by a Gaussian  $G(\bar{\varphi}, V_{\bar{\varphi}})$  for each value of  $\bar{\varphi}$

$$R^{(2)}(\bar{\varphi}, \varphi_{\text{geo}}) = I_{\bar{\varphi}} G(\bar{\varphi}, V_{\bar{\varphi}}) \Delta_{\varphi_{\text{geo}}} \quad (22)$$

and replacing  $R^{(3)}$  in Eq. 21 according to Eq. 18

$$\log L = \sum_{ie} \log \left( \sum_j \frac{G_{ie,j} f_j}{\sin \varphi_{\text{geo}}} \right) + \sum_{ie} \log \frac{I_{\bar{\varphi}} d\chi d\psi \cos \psi}{2\pi} - \sum_j T_j f_j + C \quad (23)$$

where  $T_j = \sum_{id} R_{id,j}^{(3)}$  is the sensitivity to the  $j^{\text{th}}$  pixel in the object region and the second term is a constant since the parameters  $I_{\bar{\varphi}}$ ,  $\chi$ ,  $\psi$  do not change for each event. Eq. 23 is therefore simplified as

$$\log L = \sum_{ie} \log \left( \sum_j \frac{G_{ie,j} f_j}{\sin \varphi_{\text{geo}}} \right) - \sum_j T_j f_j + C \quad (24)$$

which is the likelihood function in list mode. We are also applying a Newton-Raphson algorithm to maximize the list-mode likelihood function in equation 24.

## 4 Imaging results

The Maximum Likelihood imaging techniques in list mode has been used to produce images of calibration  $\gamma$ -ray sources. Fig. 17 shows the energy spectrum obtained from exposing LXeGRIT to a 2738 kBq  $^{88}\text{Y}$  source at a distance of 2 m, on axis, for about 90 minutes; 3-site events have been selected. Before any selection, the main features in the energy spectrum are the two  $^{88}\text{Y}$  lines (0.898 and 1.836 MeV), together with a continuum which extends up to  $\sim 3.7$  MeV due to partially absorbed  $\gamma$ -rays and, above 1.836 MeV, to pile-up of independent  $\gamma$ -rays. The energy spectrum after selecting events in the ARM peak (a selection also called software collimation) has been superimposed. The continuum is reduced by a factor of 4 at 1.5 MeV and to a negligible fraction

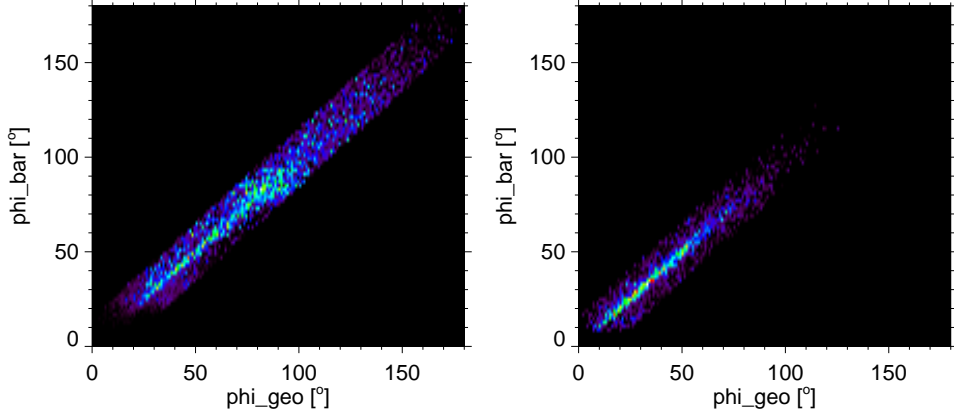


Fig. 16.  $R^{(2)}(\bar{\varphi}|\varphi_{\text{geo}})$  or point-spread function (PSF) for LXeGRIT, as obtained for MC data for a Crab-like source (i.e. with a power law energy spectrum with index 2 in the energy band from 1 to 10 MeV)  $25^\circ$  off-axis. The PSF is given by the probability of detecting  $\bar{\varphi}$  (phi\_bar) for each  $\varphi_{\text{geo}}$  (phi\_geo). *Left*: 2-site events. *Right*: 3-site events.

above 2 MeV. The intensity of the 1.836 MeV line is reduced by 45% by the ARM cut, consistent with the results presented in Sec. 3. The  $z$  and energy distributions for each of the three interactions are shown in Fig. 18, for events in the 1.836 MeV full energy peak and after software collimation. The same distributions from MC data reproducing the experimental conditions have been superimposed. The shape of the  $z$  distributions are as expected for a source on top of the detector, given that the first scatter is most likely in the forward direction. The image of the source for the 1.836 MeV line is shown in Fig. 19, reconstructed with a list mode Newton-Raphson algorithm. The source location is correctly determined with an accuracy of about one pixel, i.e.  $1^\circ$ .

A second example is the resolved image of two calibration sources,  $^{60}\text{Co}$  (1.17 and 1.33 MeV) and  $^{22}\text{Na}$  (1.27 MeV). The two sources were placed  $\sim 1.7$  m above the detector with angular separation of  $\sim 10^\circ$ . A flat diffuse background and 100% detection efficiency  $T_j$  for each pixel in the object region were assumed, together with a variance of  $V_{\bar{\varphi}}=3.5^\circ$ .

## Conclusions

LXeGRIT is the first fully developed and tested prototype of Compton Telescope based on a single position sensitive detector, such as a LXeTPC with combined event energy and 3D localization in one large homogeneous volume. In this paper the details of its performance in imaging MeV  $\gamma$ -ray sources have been presented. LXeGRIT has shown good performance as a  $\gamma$ -ray imager,

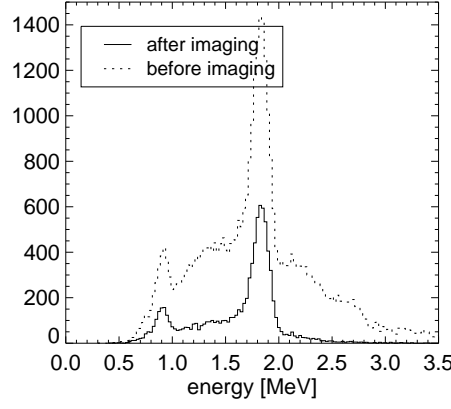


Fig. 17.  $^{88}\text{Y}$  3-site energy spectrum before and after software collimation.

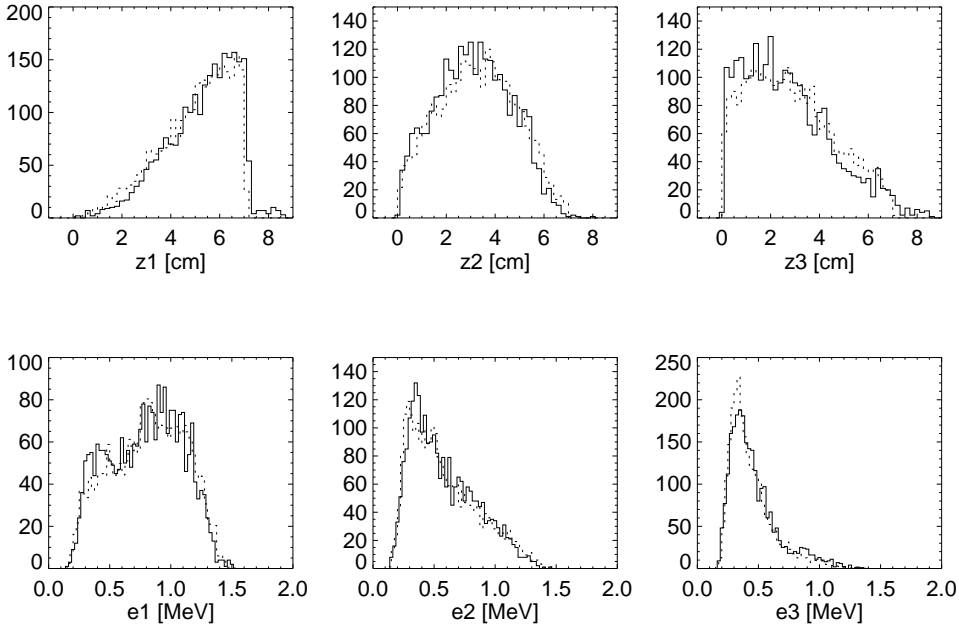


Fig. 18. Multi-site events selecting the 1.836 MeV line and applying software collimation. *Top*:  $z$  distribution for the first, second and third interaction. *Bottom*: energy spectra for the first, second and third interaction.

achieving an angular resolution of  $\sim 4^\circ$  at 1.8 MeV, consistent with expectations based on energy resolution, position resolution and geometry of its TPC. Maximum Likelihood imaging techniques have been successfully applied to the LXeGRIT data.

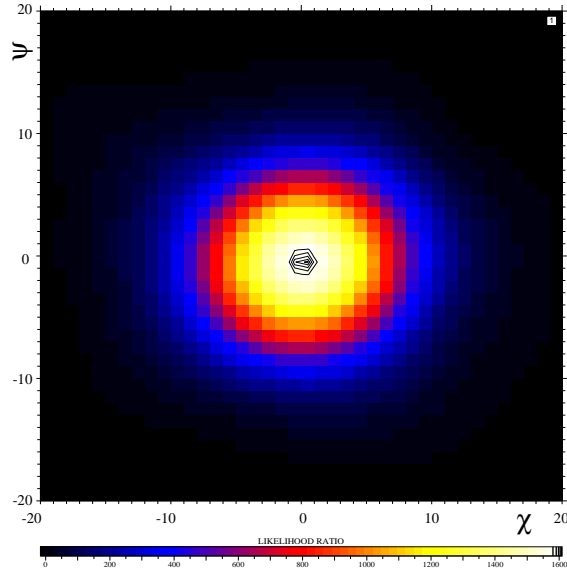


Fig. 19. Maximum likelihood (list mode) image of an  $^{88}\text{Y}$  source 2 m above the detector.

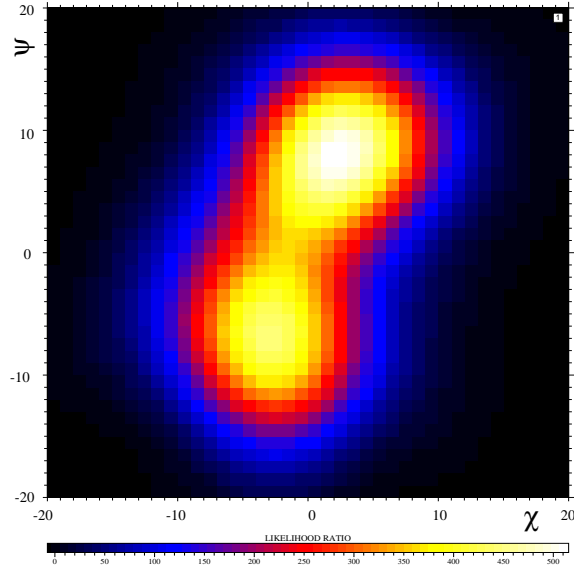


Fig. 20. Maximum likelihood (list mode) resolved image of two calibration sources,  $^{60}\text{Co}$  and  $^{22}\text{Na}$ .

## Acknowledgments

This work was supported by NASA grant NAG5-5108 to the Columbia Astrophysics Laboratory. S. Zhang acknowledges support by the Special Funds for Major State Basic Research Projects and by the National Natural Science

Foundation of China via 10733010 and KJCX2-YW-T03.

## References

- [1] U. G. Oberlack, Ph.D. Dissertation Thesis, Technische Universität München, Germany (1997)
- [2] A. Curioni, Ph.D. Dissertation Thesis, Columbia University (2004)
- [3] A. Curioni et al., Nucl. Instr. and Meth. A 576 (2007) 350
- [4] E. Aprile et al., Nucl. Instr. and Meth. A 412 (1998) 425
- [5] E.W. Lemmon, M.O. McLinden and D.G. Friend, "Thermophysical Properties of Fluid Systems" in NIST Chemistry WebBook, NIST Standard Reference Database Number 69, Eds. P.J. Linstrom and W.G. Mallard, June 2005, National Institute of Standards and Technology, Gaithersburg MD, 20899 <http://webbook.nist.gov>
- [6] XCOM: Photon Cross Sections Database, NIST Standard Reference Database 8 <http://physics.nist.gov/PhysRefData/Xcom/Text/XCOM.html>
- [7] T. Doke et al., Nucl. Instr. and Meth. A 291 (1990) 617
- [8] T. Takahashi et al., Phys. Rev. A12 (1975) 1771
- [9] U. G. Oberlack et al., *in preparation*
- [10] E. Aprile et al., Nucl. Instr. and Meth. A 302 (1991) 177
- [11] U. G. Oberlack et al., Vol. 4141 of Proc. of SPIE (2000) 168
- [12] S.E. Boggs and P. Jean, A&AS 145 (2000) 311
- [13] G. J. Schmid et al., Nucl. Instr. and Meth. A 430 (1999) 69
- [14] J. van der Marel and B. Cederwall, Nucl. Instr. and Meth. A 437 (1999) 538
- [15] K. Hagiwara et al., Phys. Rev. D66 (2002) 010001
- [16] A. Zoglauer and G. Kanbach, Vol. 4851 of Proc. of SPIE (2003) 1302
- [17] W.H. Press et al., "Numerical Recipes in Fortran", Cambridge University Press (1992)
- [18] H. de Boer et al., in *Data Analysis in Astronomy IV*, eds. V. Di Gesù, et al. , Plenum Press, New York (1992) 241
- [19] H.H. Barrett, L. Parra and T.J. White, J. Optical Soc. Amer. A (1997) , vol. 14 , no. 11